

Object-adapted optical trapping and shape-tracking of energy-switching helical bacteria

Matthias Koch¹ and Alexander Rohrbach^{1,2*}

Optical tweezers are a flexible manipulation tool used to grab micro-objects at a specific point, but a controlled manipulation of objects with more complex or changing shapes is hardly possible. Here, we demonstrate, by time-sharing optical forces, that it is possible to adapt the shape of the trapping potential to the shape of an elongated helical bacterium. In contrast to most other trapped objects, this structure can continuously change its helical shape (and therefore its mechanical energy), making trapping it much more difficult than trapping tiny non-living objects. The shape deformations of the only 200-nm-thin bacterium (*Spiroplasma*) are measured space-resolved at 800 Hz by exploiting local phase differences in coherently scattered trapping light. By localizing each slope of the bacterium we generate high-contrast, super-resolution movies in three dimensions, without any object staining. This approach will help in investigating the nanomechanics of single wall-less bacteria while reacting to external stimuli on a broad temporal bandwidth.

Optical traps have proven to be a powerful tool for the manipulation of atoms, mesoscopic objects such as beads and organelles, biological cells and even objects with sizes larger than 0.1 mm. Typically, a larger object is grabbed by one or more point traps at its edges, whereas a smaller object is grabbed as a whole. Several techniques have been used to generate more complex optical potential landscapes by shaping the trapping light from a single laser beam either holographically or by time multiplexing¹. However, adaptation of the trapping and tracking volume to the shape of the object, that is, distributing the optical energy smoothly across the extended object, has not yet been realized.

In microscopy, all structural information about an object is averaged out inside a diffraction-limited focus, so subwavelength-sized object details can be revealed only with super-resolution fluorescence techniques^{2,3}. Super-resolution requires an increase in contrast at high object frequencies. Contrast can be enhanced in interferometry and holography^{4,5}, where weakly scattered electromagnetic fields are massively amplified by the incident field of a laser beam. Several optical tweezer systems utilize a focused laser beam for both trapping and interferometric tracking of small structures. By directly measuring the interference part of the incident and scattered fields in Fourier space, very sensitive three-dimensional particle tracking has become possible^{6,7}. Back-focal plane interferometry has been successfully applied to the position tracking of single spheres^{8–10} and rods^{11,12}, but not to more complicated structures or to shape-tracking of objects.

Over the past decade, a strong interest has emerged in investigating small and relatively simple living cells such as bacteria, which serve as model systems for environmental signal processing. Advanced photonic measurement techniques are needed to understand the nanomechanics, locomotive principles and motility of bacteria, and to link these physical parameters to the spreading of bacterial diseases and their pathogenesis¹³. These techniques must be able to extract information about bacterial forces and dynamics with more detail than is possible with conventional approaches using optical point traps together with relatively simple tracking schemes^{14–18}.

Among the many different kinds of bacteria, the genus of *Spiroplasma* is of special interest because it lacks a cell wall and, accordingly, most antibiotics do not act on it. Furthermore,

Spiroplasma are often extremely small, and have a helical shape that changes quickly and in a complex manner^{19–21}. This means that they are difficult to investigate with light microscopes, which are usually too slow and have a limited depth of field with which to observe their chaotic locomotion in three dimensions. By interpreting results from electron microscopy, it has been hypothesized only recently that *Spiroplasma* are responsible for mad cow disease and Creutzfeldt–Jakob disease, rather than misfolded proteins (prions)²².

Here, we demonstrate how a light tube generated by a line-scanning optical trap can be used to stably hold and orient an ultra-small, shape-changing helical bacterium for several minutes. By coherent scattering of trapping laser light at the bacterium it is possible to achieve three-dimensional super-resolution imaging with nanometre precision at up to a kilohertz rate, thereby enabling investigation of its complex dynamics. We show how the movements can be analysed by a motility mode decomposition of the shape-changing helical structure and by energy variations, defined by switching between ground and excited mechanical energy states.

The helical bacterium

The investigated helical bacterium, *Spiroplasma melliferum*, can switch its shape, predominantly between five different modes. In the relaxed (or ground) mode, the idealized shape of the bacterium resembles a relaxed spring, which has no energy stored. However, if this spring is locally deformed (modes 1–4), mechanical energy is stored, which we define as an excited state of mechanical energy. It is our aim to optically measure, theoretically describe and quantify the switches in mechanical energy between these modes, which result from the geometrical reconfiguration of the cytoskeleton and the cell membrane. Because *Spiroplasma melliferum* lacks a stiff cell wall, it is highly deformable. The bacterium can respond to soft mechanical forces and is very sensitive to environmental influences such as changes in pH value or drug gradient²³. Without consuming energy, the cell body is almost ideally helical, which we define as the energetic ground state, because the deformational mechanical energy of the bacterium is minimal. Possibly through hydrolysis of adenosine triphosphate (ATP) molecules, the helical bacterium can transform into different shape or motility modes with local

¹Laboratory for Bio- and Nano-Photonics, Department of Microsystems Engineering-IMTEK, University of Freiburg, 79110 Freiburg, Germany,

²Centre for Biological Signalling Studies (BIOSS), University of Freiburg, 79104 Freiburg, Germany. *e-mail: rohrbach@imtek.de

changes in the helix amplitude, frequency or phase, in addition to a simple cell rotation around the long axis of the body²⁴. The most prominent motility mode is a repeated change in handedness of the helical cell body, which is always connected with a kink travelling along the cell body and is used to push the cell forward (Supplementary Movies S3 and S4, Supplementary Section S1)^{19,25}.

To understand the complex movement, we quantified the shape and temporal deformation of the bacterium by defining a three-dimensional vector function $\mathbf{c}_{\text{gs}}(x) = (x, c_y(x), c_z(x))$ of the helical centreline in the relaxed or ground state (gs), with the long axis of the cell in the x -direction (Fig. 1a, inset). The ground-state centreline \mathbf{c}_{gs} can be transformed by a matrix operation $\mathbf{c}_{\text{exc}}(t) = \hat{M}(t) \cdot \mathbf{c}_{\text{gs}}$ into an energetically excited state (exc) with time-varying vector function $\mathbf{c}_{\text{exc}}(t)$, where the excited energy is possibly provided by ATP consumption. If no energy G_{ATP} is consumed, for example, when the bacterium is dead, the shape transition matrix $\hat{M}(x, t, G_{\text{ATP}} = 0) = 1$ turns into the unity matrix. Each time the helical bacterium is deformed, $\hat{M}(x, t, G_{\text{ATP}})$ changes. We note for the deformed centreline

$$\begin{aligned} \mathbf{c}_{\text{exc}}(x, t) &= \hat{M}(x, t) \cdot \mathbf{c}_{\text{gs}}(x) = \hat{M}(x, t) \cdot (c_x, c_y, c_z)(x) \\ &= \hat{M}(x, t) \cdot (x, R \cos(k_h x), R \sin(k_h x)) \end{aligned} \quad (1)$$

where $d = 200$ nm is the body thickness, $R \approx 0.18$ μm is the mean radius of the cell body helix, $L = 3\text{--}8$ μm is the projected length of the cell body, which typically has $N = 3, \dots, 9$ periods with a mean period length of $p \approx 0.87$ μm , $k_h = 2\pi/p$ is the spatial

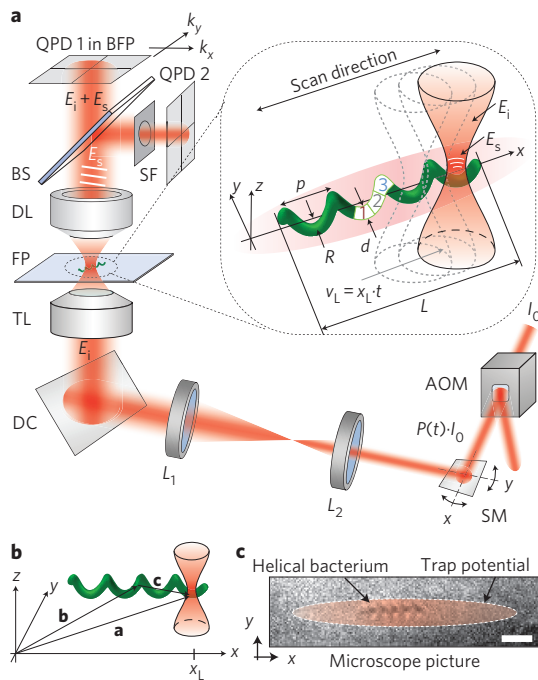


Figure 1 | Principles of space-variant trapping and tracking of a complex three-dimensional structure. **a**, The laser focus is displaced by scan mirrors (SMs) in the x -direction across the helical bacterium (body diameter d ; projected length L ; helical pitch p ; centreline radius R in the focal plane, FP). The laser beam passes an AOM, lenses (L_1, L_2), a dichroic (DC) mirror and the trapping lens (TL). QPDs with spatial filters (SFs) in the BFP of the detection lens (DL) record the interference patterns of the incident field E_i with the field E_s scattered at each segment (1, 2, 3) of the bacterium (see inset). **b**, Coordinate system for a bacterium with centreline vector $\mathbf{a}(x) = \mathbf{b} + \mathbf{c}(x)$ and laser trap position x_L . **c**, Brightfield image of bacterium trapped in a light tube (red shaded ellipse). Scale bar, 2 μm .

frequency of the helix, and $x \in [0; L]$. For further details see Supplementary Section S1.

Space-resolved object-adapted optical trapping

Optical forces, arising from light scattering at the bacterium, allow a controlled orientation and observation of the whorled bacterium. Usually, structures orient in an optical trap in a way such that the overall polarizability is maximized. The overall or average polarizability is controlled by the overlap of the focus intensity and the structure volume. Consequently, the bacterium and most other structures would be oriented along the optical axis of a conventional point trap, with nearly all spatial information about the structure and optical forces being averaged over the structure volume. A solution to this problem is to generate a horizontal, space-resolved optical trap by sweeping the laser focus back and forth, which results in an effective optical force $\mathbf{F}_{\text{opt}}(\mathbf{b})$ and potential $W_{\text{opt}}(\mathbf{b})$ relative to the centre of mass of the bacterium at position \mathbf{b} .

In most optical trapping applications, the optical force acting on a particle can be separated into a gradient force, which is to be maximized, and a scattering force (radiation pressure)²⁶, which is negligible for small particle diameters, as in our case (d much less than λ). Here, we generated an elongated area of high-intensity gradients by time-sharing the laser focus along the body of the bacterium, thus smoothly distributing the optical energy on average over time (Fig. 1c). The resulting optical gradient force $\mathbf{F}_{\text{grad}}(\mathbf{r})$ is directly proportional to the local gradient $\nabla I(\mathbf{r})$ of the focal intensity and to a Gaussian modulation of the laser intensity $P(\mathbf{r}_L(t)) = P_0 \cdot \exp(-[x_L(t)]^2/\sigma^2)$ as derived in Supplementary Section S4. Now, each point of the helical centreline of the bacterium is expressed by the vector $\mathbf{a}(x) = \mathbf{b} + \mathbf{c}(x)$, with centre-of-mass position \mathbf{b} (Fig. 1b). Therefore, the force on a cell body centre point $\mathbf{c}(x)$ of the bacterium with displacement vector \mathbf{b} is defined by the intensity gradient $\nabla I(\mathbf{a})$ relative to the laser focus at position $\mathbf{r}_L(t) = \mathbf{v}_L \cdot t$. The point force roughly acting over the focal width $\delta x \approx \lambda/2$ is $\mathbf{F}_{\text{grad}}(\mathbf{r}_L(t), \mathbf{a})$, and so the time-average $\hat{\mathbf{F}}_{\text{opt}}(\mathbf{a}) = \langle \mathbf{F}_{\text{grad}}(\mathbf{a}) \rangle$ over the scan duration $T_S = (2f)^{-1}$ can be estimated as

$$\begin{aligned} \hat{\mathbf{F}}_{\text{opt}}(\mathbf{a}(x)) &\approx \frac{\alpha n}{2cT_S} \int_0^{T_S} P(\mathbf{v}_L \cdot t) \cdot (\nabla I)(\mathbf{a}(x) - \mathbf{v}_L \cdot t) dt \\ &\approx (\kappa_{\text{opt},x} \cdot a_x, \kappa_{\text{opt},y} \cdot a_y, \kappa_{\text{opt},z} \cdot a_z) = \hat{\kappa}_{\text{opt}} \cdot \mathbf{a}(x) \end{aligned} \quad (2)$$

Here, $\hat{\kappa}_{\text{opt}}$ is the (diagonal) trap stiffness matrix, α denotes the constant polarizability of the cell body at position $\mathbf{a}(x)$ relative to the focus centre at \mathbf{r}_L , c/n is the speed of light in the cell medium with refractive index $n \approx 1.34$. When the laser focus is scanned at speeds $v_L \approx 2\Delta X f > 1$ mm s^{-1} , the bacterium trapped in water hardly experiences the sweeping point trap (that is, the force kicks are negligible) and an optical line trap, due to a time-averaged or effective optical force $\hat{\mathbf{F}}_{\text{opt}}(\mathbf{a}) = 1/T \cdot \int \mathbf{F}_{\text{grad}}(\mathbf{r}_L(t), \mathbf{a}) dt$, forms^{9,27,28}. Here, a scan frequency of $f = 400$ Hz and a sweeping range of $\Delta X = 12$ μm result in $v_L \approx 9.6$ mm s^{-1} .

Tracking local phase changes is key to achieving super-resolved images with high contrast. As illustrated in Fig. 1c, the slopes of the helical bacterium can hardly be resolved laterally with conventional incoherent imaging, although the bacterium is oriented in the focal plane by the optical trap. In the axial direction no spatial information can be extracted on the scale of the diameter of the bacterium. Using incoherent point scanning microscopy, the maximum width k_{max} of the optical transfer function is already doubled, although the modulation contrast is very bad at frequencies close to k_{max} . In coherent scanning microscopy, however, the resolution can also be approximately doubled because of the interferometric amplification of the high frequency of the scattered field. While the laser scans across the centreline of the bacterium, light is

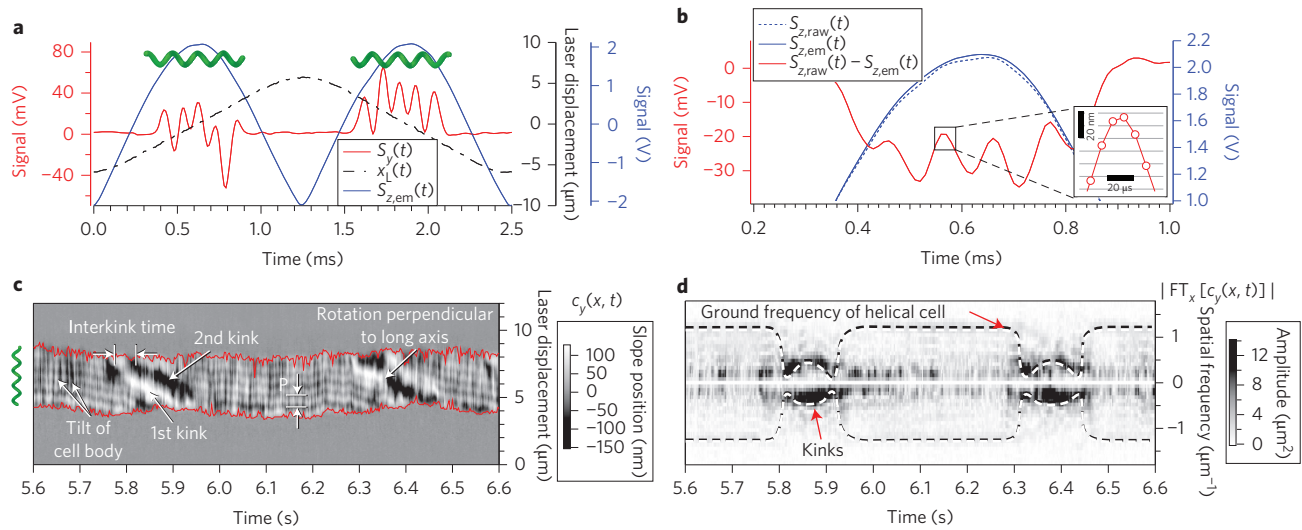


Figure 2 | Interferometric tracking signals varying with time. **a**, The position of the laser focus $x_L(t)$ is scanned back and forth (black curve) to produce a QPD raw signal $S_{y,raw}(t) = S_y(t)$ (red curve) and an empty scan z -signal $S_{z,em}(t)$ (blue curve). **b**, The difference between $S_{z,raw}(t)$ (blue dotted curve) and $S_{z,em}(t)$ (blue solid curve) results in the true z -signal $S_z(t) = S_{z,raw}(t) - S_{z,em}(t)$ (red curve). Inset: an axial tracking precision of ~ 5 nm. **c**, Kymograph of centreline $c_y(x, t)$ showing two kink pairs. **d**, Kymograph of the linewise Fourier-transformed complex signal $c_y(x, t) + ic_z(x, t)$, revealing ground and kink modes.

scattered differently at each segment of the bacterium as indicated in the inset of Fig. 1a. Detectable changes in the slope of the bacterium can be much smaller than the diameter of a diffraction-limited focus, because the tracking precision is determined mainly by the signal-to-noise ratio and not by the wavelength. The tiny phase changes $\varphi_s(\mathbf{c}(x))$ of light scattered at the slopes of the bacterium enable the determination of the degree of mechanical deformation and therefore the switching between ground and excited states of mechanical energy. The phase $\varphi_s(\mathbf{c}(x))$ encoding the three-dimensional shape $\mathbf{c}(x)$ and the centre position \mathbf{b} of the bacterium is obtained from the interference pattern $\tilde{I}(k_x, k_y, x, \mathbf{c}(x)) = |\tilde{\mathbf{E}}_i(k_x, k_y, x) + \tilde{\mathbf{E}}_s(k_x, k_y, x, \mathbf{c}(x))|^2$ between the scattered and unscattered field, $\tilde{\mathbf{E}}_s(\mathbf{c})$ and $\tilde{\mathbf{E}}_i$, in the back-focal plane (BFP) of the detection lens (Fig. 1a). When the focused laser sweeps from left to right along $x(t)$, interference intensities $\tilde{I}(x(t), \mathbf{c}(x))$ are recorded at a typical sampling rate of 100 kHz corresponding to a spatial sampling of 96 nm using a sweeping scan rate of $f = 400$ Hz, that is, when 800 scans per second are performed across the bacterium. The sampling frequency of $(96 \text{ nm})^{-1}$ is more than two times higher than the largest object frequency and therefore does not cause the image quality to deteriorate. From the BFP interference intensity $|\tilde{\mathbf{E}}_i + \tilde{\mathbf{E}}_s(\mathbf{c})|^2 = \tilde{I}_i + \tilde{I}_s(\mathbf{c}) + 2\text{Re}\{\tilde{\mathbf{E}}_i^* \cdot \tilde{\mathbf{E}}_s(\mathbf{c})\}$ the correlation term containing the phase shifts $\varphi_s(\mathbf{c}(x))$ reads

$$\begin{aligned} \text{Re}\{\tilde{\mathbf{E}}_i \cdot \tilde{\mathbf{E}}_s^*(\mathbf{c})\} &= \frac{1}{2} (|\tilde{\mathbf{E}}_i + \tilde{\mathbf{E}}_s(\mathbf{c})|^2 - |\tilde{\mathbf{E}}_i|^2) \\ &= |\tilde{\mathbf{E}}_i| \cdot |\tilde{\mathbf{E}}_s^*(\mathbf{c})| \cdot \text{Re}\{\exp(i\varphi_s - i\varphi_i(\mathbf{c}))\} \\ &\approx A \cdot \sin(\Delta\varphi_s(\mathbf{c})) \end{aligned} \quad (3)$$

where the phase difference $\Delta\varphi_s(\mathbf{c}) = (\varphi_s(\mathbf{c}) + \pi/2) - \varphi_i$ contains the $\pi/2$ phase delay of the Rayleigh-scattered field relative to the incident. The constant factor $A = |\tilde{\mathbf{E}}_i^*| \cdot |\tilde{\mathbf{E}}_s(\mathbf{c})|$ indicates the nearly constant contrast intensity over the length of the bacterium. The series of interference patterns is recorded by the two quadrant photodiodes (QPDs) in the BFP of the detection lens (DL; Fig. 1a). Remarkably, no relevant bacterial shape information is lost, although the interference intensity is integrated by only four detectors of the QPD (for details, see the Methods). For each segment x of the bacterium centreline $\mathbf{a}(x) = \mathbf{b} + \mathbf{c}(x)$, the corresponding position signal $\mathbf{S}(\mathbf{a})$ on the QPD is defined by the

difference of a signal $\mathbf{S}_{raw}(\mathbf{a})$ with scatterer and a signal \mathbf{S}_{empty} without scatterer:

$$\begin{aligned} \mathbf{S}(\mathbf{a}(x)) &= \mathbf{S}_{raw}(\mathbf{a}(x)) - \mathbf{S}_{empty} \\ &\approx 2P(x) \cdot \iint_{A_{BFP}} |\tilde{\mathbf{E}}_i| |\tilde{\mathbf{E}}_s(\mathbf{a})| \cdot \sin(\Delta\varphi(\mathbf{a}(x))) \cdot \mathbf{H} \, dA \\ &\approx \vec{g} \cdot \mathbf{a}(x) = \vec{g} \cdot \mathbf{b} + \vec{g} \cdot \mathbf{c}(x) \end{aligned} \quad (4)$$

Here, \vec{g} is the (diagonal) detector sensitivity matrix, $\mathbf{H}(k_x, k_y, \text{NA}_{det})$ is a spatial filter function (see Methods). As pointed out in equations (3) and (4), the intensity of the unscattered, incident light $P(x) \cdot |\tilde{\mathbf{E}}_i|^2$ resulting in the signal \mathbf{S}_{empty} needs to be subtracted from the measured signal \mathbf{S}_{raw} . These intensities are modulated by the transmission $P(x)$ of the acousto-optical modulator (AOM) to generate a harmonic optical line trap. \mathbf{S}_{raw} must be recorded separately without the bacterium in the trap ('empty' trap). Remarkably, the position signals are approximately linear for small displacements $\mathbf{a}(x)$, such that the position of one segment of the bacterium is simply $a_j(t) \approx S_j(t)/g_j$ ($j = x, y, z$). Because the signal strength and linearity depend on NA_{det} of the detection lens²², we use two QPDs with two different spatial filters for lateral and axial bacterial displacements, as shown in Fig. 1a.

As introduced above, the local phase delay $\Delta\varphi(x) = \mathbf{a}(x) \cdot \Delta\mathbf{k} = \mathbf{a}(x) \cdot (\mathbf{k}_s - \mathbf{k}_i)$ induced by the bacterium encodes the shape and energy switching of the helical bacterium, which are described by the elements of the shape transition matrix $M_{j,k}$ (see equation 1). This is one of the key findings of our Article:

$$\Delta\varphi(x) = \Delta\mathbf{k} \cdot (\mathbf{b} + \vec{M}(x) \cdot \mathbf{c}_{gs}(x)) \quad (5)$$

Measuring $\Delta\varphi$ allows recovering $c_{exc,j}(x) = \sum M_{j,k}(x) \cdot c_j(x)$ in addition to \mathbf{b} , thereby unravelling the bacterial motility mode changes expressed by $M_{j,k}(x)$, (direction $j = x, y, z$).

Results

The object adapted optical potential distributes the optical energy smoothly across the helical bacterium and allows it to be held and oriented, which would not be possible with static point traps. Sweeping the point trap back and forth at 400 Hz along a line

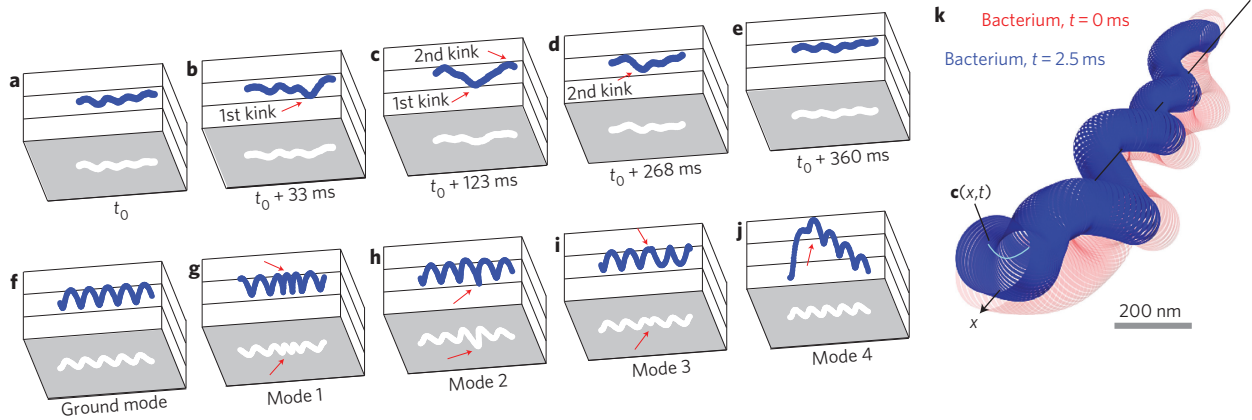


Figure 3 | Three-dimensional representation of measured and simulated shape deformations. **a–e**, Time series of a measured double kink cycle. Kinks are indicated by red arrows. **f–j**, Simulations showing five possible elementary shape modes $c^{(m)}$ of a helical structure: ground mode $m=0$, an unperturbed helix (**f**); partial helix compression (**g**); partial change of the helix amplitude (**h**); change of the helicity of the helix (**i**); helix kink (**j**). **k**, Measured body centreline of the bacterium at two time points, $c(t=0)$ in red and $c(t=2.5\text{ ms})$ in blue. The diameter of the bacterium was assumed to be 200 nm.

also allows measurement of the space-resolved local displacements and forces of the deforming body $c(x)$.

Centreline projections

As a result of the focus sweep, Fig. 2 illustrates the measured QPD signals, which are components of the parametric representation $(t, S_y(t), S_z(t))$ of the images $S(x(t)) \approx \vec{g} \cdot c(x(t))$ of the centreline of the bacterium. Figure 2a,b shows the signals from the ‘empty scan’ $S_{z,em}(t) = P(t) \cdot |\vec{E}_i|^2$ without the bacterium, which is the incident intensity $|\vec{E}_i|^2$ modulated by a Gaussian transmission function $P(v_L \cdot t) = P_0 \cdot \exp(-v_L \cdot t)^2 / \sigma^2$. It further shows the raw z -signal $S_{z,raw}(t)$, which also contains the unscattered light, and the final z -signal $S_z(t) = S_{z,raw}(t) - S_{z,em}(t)$ according to equation (4), which encodes the time-varying centre position $b(t)$ and the shape of the bacterium $c(t)$. The centreline projection is plotted as the lateral y -signal $S_y(t)$ in Fig. 2a and as the axial z -signal $S_z(t)$ in Fig. 2b. The position x of the laser is steered by scan mirrors and moves back and forth with the dominant velocity $v_L = \Delta x_L / \Delta t$, which is indicated by the black line in Fig. 2a. The small difference between the dotted and solid blue curves in Fig. 2b indicates how tiny the scattering signal is. However, the wavy position signals from the bacterium are clearly visible with a precision of 5–10 nm (Fig. 2b, inset) and can be 12 bit-digitized without notable shot noise due to the high photon densities. The three-dimensional coherent optical image is only affected by the spatial period p of the bacterium, which causes a deterioration in the tracking precision for $p < \lambda/2$, when calibration errors Δg_y and Δg_z increase (Supplementary Section S5).

Time evolution

To understand the nanomechanics and motility of the bacterium, kymographs were used to visualize and analyse its shape deformations. Kymographs $c(x, t) \sim S(x, t)$ show the projection of the centreline $c(x)$ on one axis as a function of time t . In this way, the time evolution of the motility modes can be well observed in a two-dimensional plot, either in real space as $c_i(x, t)$ or in Fourier space as $|\text{FT}_x[c_i(x, t)]|$, where $i = y, z$ are the directions perpendicular to the central x -axis. Both Fig. 2c and d allow identification of the ground frequency $k_h = 2\pi/p$ of the helical cell with period p (Fig. 1a), as well as the most pronounced motility mode, the kink mode, which manifests itself by a strong amplitude and low spatial frequency. However, the wavy position signals $S_y(t)$ and $S_z(t)$ are subject to Brownian noise and are sometimes difficult to interpret. We therefore performed computer simulations to understand the generation of the resulting motility signals $S_y(c(t))$ and $S_z(c(t))$ and therewith the image of the bacterium. As further

explained in Supplementary Section S1, motility modes were simulated for all five known shape deformation modes $c^{(m)}(x) = M^{(m)}(x) \cdot c_{gs}(x)$ ($m=0, \dots, 4$), revealing that the kink mode ($m=4$) provides the strongest signals. This is illustrated in Fig. 3, where signals $S_y(t)$ and $S_z(t)$ have been plotted against each other along time $t = x_L / v_L$ for one single laser scan, resulting in the image of the body line $c(x, S_y(x)/g_y, S_z(x)/g_z)$ with a structural information content that is clearly beyond conventional image resolution (Fig. 3k). The first row in Fig. 3 describes the time evolution of a measured double kink (Supplementary Movie S3), and the second row the simulated motility modes.

Bacterial energy fluctuations

To estimate the energy of the bacterium in the excited state relative to the ground state, the shape deformation $\Delta c(x) = c_{exc}(x) - c_{gs}(x) = (M(x) - 1) \cdot c_{gs}(x)$ and the restoring forces $F(x)$ at each point x need to be measured. The displacement of each body element $\Delta c(x) = (0, \Delta c_y, \Delta c_z)$ is perpendicular to the central x -axis. The total force is the sum of the internal mechanical forces $F_{mec}(x) \approx \kappa_{mec}(x) \cdot \Delta c(x)$ of the bacterium (due to bending of membranes and filaments), the hydrodynamic friction forces $F_y(x) = \gamma_{yz} \Delta c(x) / \tau$ and the optical forces $\hat{F}_{opt}(x) \approx \vec{\kappa}_{opt} \cdot \Delta c(x) \gg F_y(x)$ (see equation (2)). Estimates of these forces as well as the calibration constants g_j for the detector and $\kappa_{opt,j}$ for the trap ($j = x, y, z$) are explained in Supplementary Section S5.

Across the focal width of $\delta x \approx \lambda/2$, the energy $W(x)$ is the product of the total force $F_{tot}(c(x))$ and the displacement such that $W(x) = F_{tot}(c(x)) \cdot c(x) = 1/2 \kappa_y \cdot c_y(x)^2 + 1/2 \kappa_z \cdot c_z(x)^2$. Hence, the energy needed to displace a body element from c_{gs} to c_{exc} is approximately $W_{exc} - W_{gs}$. Therefore, the time-varying total energy $\Delta W(t)$ raised by the bacterium against the total force over the distance S_i/g_i is integrated over the length L of the bacterium:

$$\begin{aligned} \Delta W(t) &= W_{exc}(t) - W_{gs} \\ &\approx \frac{2}{\lambda} \int_0^L F_{tot}(\vec{M} \vec{c}_{gs}) \cdot (\vec{M}(x, t) c_{gs}(x)) dx - \frac{2}{\lambda} \int_0^L F_{tot}(c_{gs}) \cdot c_{gs}(x) dx \\ &\approx \frac{2}{\lambda} \int_0^L ((\kappa_{opt,y} + \kappa_{mec}) \cdot (S_y(x, t)/g_y)^2 \\ &\quad + (\kappa_{opt,z} + \kappa_{mec}) \cdot (S_z(x, t)/g_z)^2) dx - W_{gs} \end{aligned} \tag{6}$$

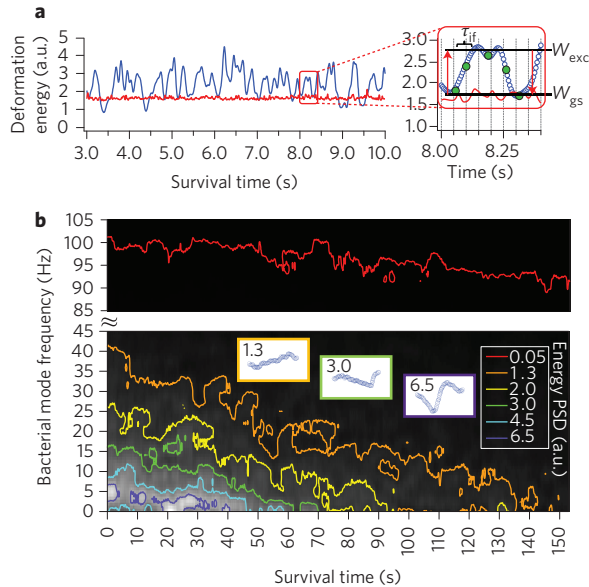


Figure 4 | Time-dependent transitions between ground and excited levels of mechanical energy. An optically trapped bacterium experiences oxidative stress until it dies after ~ 140 s. **a**, Time series $\Delta W(t) = (W_{\text{opt}}(t) + W_{\text{mec}}(t)) - W_{\text{gs}}$ of switching between energy levels W_{exc} and W_{gs} and a magnification of a typical energy slope belonging to a kink mode (right). The red level indicates the thermal energy of a dead bacterium. The arbitrary energy unit a.u. = $(10^{-3} \text{ V})^2$ corresponds to $\sim 10k_B T$ in optical energy W_{opt} . **b**, Power spectral density contour plot PSD(ω, t_s) as a function of time t_s , revealing significant energy patterns for a single bacterium exposed to oxidative stress. The red contour line at 100 Hz indicates pure thermal noise movements of the bacterium.

The energy ΔW is obtained by using the total force and the interferometric displacement signal as described by equation (4). $\Delta W = (W_{\text{opt}} + W_{\text{mec}}) - W_{\text{gs}}$ describes only relative changes, because only the optical energy W_{opt} can be measured, but the mechanical bending energy W_{mec} of the bacterium is still unknown. Assuming $\kappa_{\text{opt},y,z} \approx q_{y,z} \cdot \kappa_{\text{mec}}$, we can conclude that W_{mec} is proportional to the excited energy $\Delta W(t) + W_{\text{gs}} = W_{\text{mec}}(t) \cdot (1 + 1/q_{y,z})$ of the bacterium. As a representative application we measured a time series of the relative deformation energy $\Delta W(t)$ fluctuating between the ground state and the excited state as shown in Fig. 4a. A frequently occurring energy signal is magnified on the right, indicating the transitions between the levels of the ground state and the excited state. As evaluated by the simulations, this energy signal clearly belongs to a kink mode ($m = 4$, Fig. 3j). The corresponding shape deformation $c^{(4)}(t)$ is illustrated in Fig. 3a–e and $\Delta W(t)$ indicated in Fig. 4a (right) by five green dots.

Induced death of the bacterium

As pointed out earlier, it is of broader interest to analyse cellular reactions (such as body deformations) of a living bacterium as a function of time under various external disturbances. We therefore induced oxidative stress on the bacterium by generating reactive oxygen ions, which form as a result of increased laser light exposure²⁹. These reactive oxygen ions can be bound by adding oxygen scavengers. Without oxygen scavengers the bacterium died after ~ 140 s due to environmental stress, after the synthesis of energy-providing molecules such as ATP had stopped and energy stocks had been consumed. As a consequence, the energy patterns $\Delta W(t)$ changed in amplitude, shape and frequency as a function of survival time t_s , as shown in Fig. 4b, which plots the power spectral density PSD(ω, t_s) = $|\text{FT}[\Delta W(t, t_s)]|^2$ of the changes in

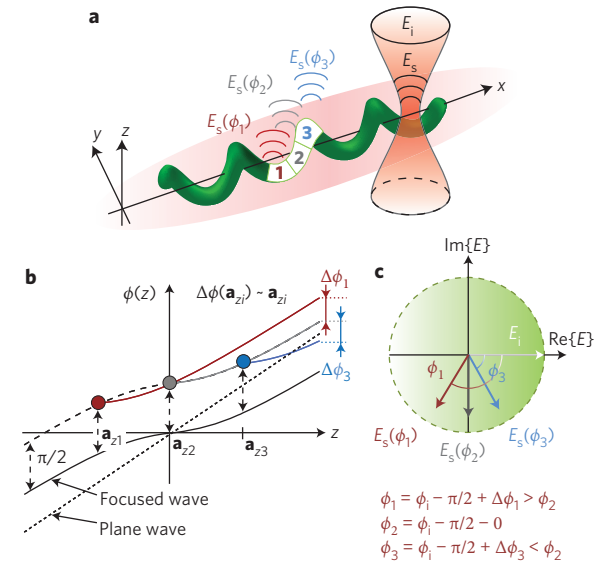


Figure 5 | Local phase changes induced by the bacterium. **a**, Schematic of light scattering at three different body position $\mathbf{a}(x) = \mathbf{a}_1, \mathbf{a}_2, \mathbf{a}_3$ of the bacterium resulting in three different scattered fields \mathbf{E}_s with phases ϕ_1, ϕ_2, ϕ_3 . **b**, Axial phase dependence for a plane wave $\phi_{\text{pw}}(z) = kz$ and for a focused wave with $\phi_{\text{fw}}(z) = kz - \text{atan}(kz \cdot \text{NA}^2/n^2)$ as well as the position-dependent phase differences $\Delta\phi(a_z) - \pi/2 = \phi_s - \phi_i(a_z) \approx a_z$ between incident field \mathbf{E}_i and scattered fields \mathbf{E}_s for large z . **c**, Phase diagram indicating the phase differences for large z .

mechanical energy of the bacterium. Although more complex analyses are possible, Fig. 4b shows that all transitions to excited states are shifted to lower frequencies as bacterial death approaches ($t_s \approx 140$ s). Only with our advanced imaging and analysis method is it possible to detect the decay of the low-energy transitions, that is, of the small deformations (PSD ≈ 1.3 a.u.) relative to the thermal noise ground-state energies (for example, PSD ≈ 0.05 a.u.). Higher-energy amplitudes (PSD > 3 a.u.), mainly belonging to kink signals (motility mode 4), occur less frequently the longer the bacterium is stressed. Strong PSD peaks during the first 50 s can be identified as an increase of motility to escape from the trap and may be an indication of a bacterial reaction to this stress (see areas where PSD > 4.5 a.u.). In this context, one should state that the mean duration of a double kink cycle of a trapped cell is 0.2 s, which is four times shorter than that of a freely swimming bacterium²¹. These findings definitely merit further investigations, which are not within the scope of this study. However, this combination of experiment and data analysis provides a new method with which to investigate the energetics of nanoscale organisms.

Discussion

We have set what we believe to be a new milestone in trapping and tracking of very small and living objects. First, the trapped helical structures are very weak light scatterers, and therefore exhibit small optical forces resulting in potential depths of $\sim 5k_B T$. Second, the helical bodies of the bacteria undergo fast shape deformations that make optical trapping and tracking much more difficult than with any other object ever stably trapped before. We have shown by experiment and theory that, for this helical structure, an effective optical potential arises in all three spatial directions by sweeping an optical point trap along a line. While oriented horizontally inside the light trap, the ultrasmall, 200-nm-thin bacterium undergoes complex and fast shape changes, which we measured pointwise with nanometre precision at rates of 800 Hz. The high tracking rate, which could be increased further, is necessary to

distinguish thermal motions arising from small active bacterial motions. Our coherent scanning technique results in three-dimensional optical images with a resolution that is clearly beyond conventional optical resolution in all three directions, revealing much more contrast than incoherent point-scanning techniques based on fluorescence principles. No staining is required and no bleaching can occur, because the tracking relies on phase differences between unscattered light and light scattered specifically for each slope of the bacterium, exploiting the position-dependent Gouy phase anomaly of focused beams. We introduced the novel concept of transitions and fluctuations in a mechanical multilevel energy system, which is described by state vectors and transition matrices. Based on this concept, it should be possible to deduce the molecular reorganizations inside the bacterium during shape changes. The time–frequency representations of fast multimode energy signals used here might enable new methods of investigating the nanomechanics of single cells reacting to external stimuli. Moreover, the technique and principles presented in this study may allow new insights into bacterial energetics and therefore the spread of bacterial diseases.

Methods

Optical set-up. The most important elements of the optical trapping and tracking unit are shown in Fig. 1a, and further details can be found in Supplementary Section S2. For object-adapted trapping and interferometric tracking, we used a highly focused 1,064 nm continuous-wave (c.w.) laser beam, which was scanned along the centre of the non-spherical object. We controlled the depth of the optical potential $V(x_i)$ by scanning the laser focus laterally along $x_i(t)$ and modulated the intensity I_0 using an AOM. The AOM generated a Gaussian profile $P(x_i(t)) = P_0 \exp(-|x_i(t)|^2/\sigma^2)$ such that the transmitted intensity was $P(x_i(t)) \cdot I_0$. In all experiments we used a power of $P_0 = 160$ mW in the point focus, resulting in a laser power of $0.6P_0 = 95$ mW distributed over the line trap with length $L = 10 \mu\text{m}$ (where $1/L \cdot \int \exp(-x^2/\sigma^2) dx \approx 0.6$). Over the length of a 4- μm -long bacterium, this corresponds to $0.36P_0 = 58$ mW. The laser focus was displaced along x_i in the focal plane of the objective/trapping lens through galvanometric scan mirrors. The tracking lens with numerical aperture $\text{NA}_{\text{tr}} = 1.2$ controlled the trap stiffnesses κ together with the AOM. The BFP of the detection lens with $\text{NA}_{\text{det}} = 0.9$ was projected by two further parallel 4f lens systems (not shown) onto two QPDs (QPD₁ and QPD₂), with different apertures $\text{NA}_{\text{det},2} = 1/2\text{NA}_{\text{det},1}$. At the BFP, the time-variant fields $\tilde{\mathbf{E}}_i(k_x, k_y, t)$ and $\tilde{\mathbf{E}}_s(k_x, k_y, t)$ interfere, and $\tilde{\mathbf{E}}_s$ is scattered specifically at each slope of the helical cell. With help of a reference diode behind the AOM and an electronic feedback system (not shown), $I_0(t)$ was stabilized to avoid artefacts in the axial tracking due to power noise. The sweeping of the laser focus along a line at several 100 Hz time-averaged the optical trapping potential (Fig. 1a, inset), but not the local phase delays due to scattering. For technical details see Supplementary Section S2.

Increase of contrast at high spatial frequencies. The significant increase in three-dimensional spatial information obtained with our imaging method is clearly visible by comparing Fig. 1c with Fig. 3 (see also the Supplementary Movies). The width of the modulation transfer function in terms of the corner frequency $k_{\text{max}} = 2\pi/\lambda \cdot (\text{NA}_{\text{tr}} + \text{NA}_{\text{det}})$ corresponds to that of a point-scanning microscope with two lenses with numerical apertures NA_{tr} and NA_{det} . The value of k_{max} was about twice that of a conventional wide-field microscope. However, due to coherent amplification, that is, due to local interferences $|\mathbf{E}_i(\mathbf{r}) + \mathbf{E}_s(\mathbf{r}, \mathbf{b})|^2$ with the incident field, the image contrast $2|\tilde{\mathbf{E}}_i||\tilde{\mathbf{E}}_s|\sin(\Delta\varphi)$ generated by the scattered field was significantly increased at the high frequencies close to k_{max} . After subtracting $I_i(\mathbf{r})$ from the intensity $I(\mathbf{r}, \mathbf{b}) = I_i(\mathbf{r}, \mathbf{b}) + [I_s(\mathbf{r}, \mathbf{b}) + 2\sqrt{I_i I_s} \sin(\Delta\varphi)]$, the remaining effective point-spread function (PSF) is bipolar because of the additional $\cos(\Delta\varphi - \pi/2) = \sin(\Delta\varphi)$ modulations, but still has about the same width as the conventional PSF $I_i(\mathbf{r})$. The bipolar PSF(b_z) reads, for example, in $z \sqrt{[I_i(b_z) \cdot I_s] \cdot \sin(k_{\text{gz}} \cdot b_z)}$ with $k_{\text{gz}} = k\text{NA}_{\text{tr}}^2/n^2 < 2\pi/\lambda$. Because of the high signal-to-noise ratio (Fig. 2b), the increase in modulation contrast at high frequencies is sufficiently large to increase the image quality considerably. However, the coherent imaging process becomes significantly more complicated for more than one scatterer³⁰ because of the coherent superposition of all scattered fields.

Tracking local phase changes by BFP interference is key to achieving high-contrast, super-resolved images of bacteria. The interference term of the angular spectrum for the ideal helix $\mathbf{c}(x)$ reads, according to equation (3),

$$\begin{aligned} \text{Re}\{\tilde{\mathbf{E}}_i \cdot \tilde{\mathbf{E}}_s^*\} &= |\tilde{\mathbf{E}}_i| \cdot |\tilde{\mathbf{E}}_s^*| \cdot \cos(\varphi_s - \varphi_i(\mathbf{c})) \\ &\stackrel{\varphi_i=0}{=} |\tilde{\mathbf{E}}_i| \cdot |\tilde{\mathbf{E}}_s^*| \cdot \sin(k_x x_L + k_y R \cos(k_i x_i) + k_z R \sin(k_i x_i)) \end{aligned} \tag{7}$$

where the phase difference $\Delta\varphi_s(\mathbf{c}) = (\varphi_s(\mathbf{c}) + \pi/2) - \varphi_i$ contains the $\pi/2$ phase delay of the Rayleigh-scattered field relative to the incident such that

$\cos(\varphi_s - \varphi_i) = \cos(\Delta\varphi_s - \pi/2) = \sin(\Delta\varphi_s)$. This interference term structures the PSF and therefore increases the width of the optical transfer function.

To measure the axial displacements of the bacterial slopes, we exploited the position-dependent Gouy phase shift, which is a result of the k -vector's average z -components $\langle k_z \rangle < 2\pi/\lambda = k = k_0 \cdot n$ in a focused beam. $\langle k_z \rangle$ leads to an extended wavelength (λ_z) or the anomalous phase retardation $\phi_{\text{fw}}(z) \approx kz - \text{atan}(kz \cdot \text{NA}^2/n^2) \in [-\pi/2; \pi/2]$ of a wave focused with NA relative to a plane wave with $\phi_{\text{pw}}(z) = kz$, as demonstrated in Fig. 5b³¹. However, the divergent field $\tilde{\mathbf{E}}_s(\mathbf{a}(x))$ scattered at each slope $\mathbf{a}(x)$ of the bacterium also experiences this phase retardation $\phi_{\text{fw}}(z - a_z) \leq \pi/2$, such that the phase profile is shifted by the axial position a_z of the scatterer, as indicated in Fig. 5b for three different positions a_{z1}, a_{z2}, a_{z3} . In addition, the scattered field is determined by the phase $\phi_{\text{fw}}(a_z)$ of the incident field such that $\phi_s(z, a_z) = \phi_{\text{fw}}(a_z) + \phi_{\text{fw}}(z - a_z)$. The phase difference between the incident focused wave and the scattered wave can be approximated as

$$\begin{aligned} \Delta\phi_s(a_z) &= \lim_{z \rightarrow \infty} (\phi_s(z, a_z) - \phi_i(z)) + \pi/2 \\ &= \pi/2 + \text{atan}(k_0 a_z \text{NA}^2/n) \\ &= \pi/2 + (k_0 \text{NA}^2/n) \cdot a_z \end{aligned} \tag{8}$$

where $\lim_{z \rightarrow \infty} (\text{atan}(k_0(z - a_z)\text{NA}^2/n) - \text{atan}(k_0 z \text{NA}^2/n)) = 0$, leading to the result that the phase difference $\Delta\phi_s(a_z(x))$ is proportional to the axial position $a_z(x)$ of one point of the bacterium at lateral position x .

Three position signals $(S_x(x), S_y(x), S_z(x))$ were recorded by two QPDs, which measured different signal strengths due to their different spatial filters (SFs) controlled by NA_{det} (Fig. 1a). However, in principle, a single QPD is sufficient, delivering $n = 1, \dots, 4$ intensity raw signals $S_n^{\text{raw}}(t)$.

The interference term contains all the three-dimensional spatial information about the shape of the bacterium and is recorded by the two QPDs in the BFP of the detection lens (Fig. 1a). More precisely, the interference pattern $P(x) \cdot \tilde{I}_i(k_x, k_y, x, \mathbf{c}(x))$ modulated with the transmission $P(x(t))$ of the AOM is imaged onto $n = 1, \dots, 4$ detector areas A_n of the QPD limited with the detection angular aperture $\sin(\alpha_{\text{det}})$. This leads to four raw signals $\hat{S}_n^{\text{raw}}(x) = P(x) \cdot \int_{A_n} \tilde{I}_i(k_x, k_y) dk_x dk_y$, which are linearly combined to a signal triplet $\mathbf{S}(x, \mathbf{a}(x)) = (S_x, S_y, S_z)$ providing a nanometre-precise three-dimensional position signal at each point x_L along the laser scan direction. After subtracting the intensity $P(x) \cdot \tilde{I}_i(x)$ of the unscattered light, the position signal can be expressed as

$$\begin{aligned} \mathbf{S}(\mathbf{a}(x)) &= P(x) \iint_{A_{\text{BFP}}} \tilde{I}_{\text{raw}}(\mathbf{a}(x)) \cdot \mathbf{H} dA - P(x) \iint_{A_{\text{BFP}}} \tilde{I}_i \cdot \mathbf{H} dA \\ &\approx \iint_{A_{\text{BFP}}} 2|\tilde{\mathbf{E}}_i||\tilde{\mathbf{E}}_s(\mathbf{a})| \cdot \sin(\Delta\varphi_s(a_x) + \Delta\varphi_s(a_y) + \Delta\varphi_s(a_z)) \cdot \mathbf{H} dA \end{aligned} \tag{9}$$

Here, the vector $\mathbf{H}(k_x, k_y, \text{NA}_{\text{det}}) = (H_x, H_y, H_z)$ is another spatial filter function defining summation or subtraction of the signals $S_n^{\text{raw}}(t)$. Subtraction of signals $S_x = (S_1^{\text{raw}} + S_2^{\text{raw}}) - (S_3^{\text{raw}} + S_4^{\text{raw}})$ is provided by H_x and $S_y = (S_1^{\text{raw}} + S_3^{\text{raw}}) - (S_2^{\text{raw}} + S_4^{\text{raw}})$ by H_y , as well as summation of the signals $S_z = \sum_{i=1}^4 S_i^{\text{raw}}$ is provided by H_z . For small particle or bacterial slope displacements $\mathbf{a}(x)$, this dependency can be approximated to be linear, such that $(S_x(a_x), S_y(a_y), S_z(a_z)) \approx \hat{\mathbf{g}} \cdot \mathbf{a} = (g_x \cdot a_x, g_y \cdot a_y, g_z \cdot a_z)$ and the detector sensitivity matrix $\hat{\mathbf{g}}$ is diagonal (for further details see Supplementary Section S3).

Received 6 February 2012; accepted 15 August 2012; published online 23 September 2012

References

- Dholakia, K. & Reece, P. Optical micromanipulation takes hold. *Nano Today* **1**, 18–27 (2006).
- Hell, S. W. Far-field optical nanoscopy. *Science* **316**, 1153–1158 (2007).
- Gustafsson, M. G. L. Surpassing the lateral resolution limit by a factor of two using structured illumination microscopy. *J. Microsc.* **198**, 82–87 (2000).
- Xu, W. B., Jericho, M. H., Meinertzhagen, I. A. & Kreuzer, H. J. Digital in-line holography for biological applications. *Proc. Natl Acad. Sci. USA* **98**, 11301–11305 (2001).
- Lee, S.-H. & Grier, D. G. Holographic microscopy of holographically trapped three-dimensional structures. *Opt. Express* **15**, 1505–1512 (2007).
- Pralle, A., Prummer, M., Florin, E.-L., Stelzer, E. H. K. & Hörber, J. K. H. Three-dimensional position tracking for optical tweezers by forward scattered light. *Microsc. Res. Tech.* **44**, 378–386 (1999).
- Rohrbach, A. & Stelzer, E. H. K. Three-dimensional position detection of optically trapped dielectric particles. *J. Appl. Phys.* **91**, 5474–5488 (2002).
- Dreyer, J. K., Berg-Sorensen, K. & Oddershede, L. Improved axial position detection in optical tweezers measurements. *Appl. Opt.* **43**, 1991–1995 (2004).
- Speidel, M., Friedrich, L. & Rohrbach, A. Interferometric 3D tracking of several particles in a scanning laser focus. *Opt. Express* **17**, 1003–1015 (2009).

10. Friedrich, L. & Rohrbach, A. Improved interferometric tracking of trapped particles using two frequency detuned beams. *Opt. Lett.* **35**, 1920–1922 (2010).
11. Kress, H., Stelzer, E. H. K. & Rohrbach, A. Tilt angle dependent three-dimensional-position detection of a trapped cylindrical particle in a focused laser beam. *Appl. Phys. Lett.* **84**, 4271–4273 (2004).
12. Irrera, A. *et al.* Size-scaling in optical trapping of silicon nanowires. *Nano Lett.* **11**, 4879–4884 (2011).
13. Min, T. L. *et al.* High-resolution, long-term characterization of bacterial motility using optical tweezers. *Nature Methods* **6**, 831–U871 (2009).
14. Rowe, A. D., Leake, M. C., Morgan, H. & Berry, R. M. Rapid rotation of micron and submicron dielectric particles measured using optical tweezers. *J. Mod. Opt.* **50**, 1539–1554 (2003).
15. Chattopadhyay, S., Moldovan, R., Yeung, C. & Wu, X. L. Swimming efficiency of bacterium *Escherichia coli*. *Proc. Natl Acad. Sci. USA* **103**, 13712–13717 (2006).
16. Dombrowski, C. *et al.* The elastic basis for the shape of *Borrelia burgdorferi*. *Biophys. J.* **96**, 4409–4417 (2009).
17. Wang, S. Y., Arellano-Santoyo, H., Combs, P. A. & Shaevitz, J. W. Actin-like cytoskeleton filaments contribute to cell mechanics in bacteria. *Proc. Natl Acad. Sci. USA* **107**, 9182–9185 (2010).
18. Ashkin, A. & Dziedzic, J. M. Optical trapping and manipulation of viruses and bacteria. *Science* **235**, 1517–1520 (1987).
19. Gilad, R., Porat, A. & Trachtenberg, S. Motility modes of *Spiroplasma melliferum* BC3: a helical, wall-less bacterium driven by a linear motor. *Mol. Microbiol.* **47**, 657–669 (2003).
20. Wolgemuth, C. W., Igoshin, O. & Oster, G. The motility of mollicutes. *Biophys. J.* **85**, 828–842 (2003).
21. Shaevitz, J. W., Lee, J. Y. & Fletcher, D. A. *Spiroplasma* swim by a processive change in body helicity. *Cell* **122**, 941–945 (2005).
22. Bastian, F. O. *et al.* *Spiroplasma* spp. from transmissible spongiform encephalopathy brains or ticks induce spongiform encephalopathy in ruminants. *J. Med. Microbiol.* **56**, 1235–1242 (2007).
23. Trachtenberg, S. & Gilad, R. A bacterial linear motor: cellular and molecular organization of the contractile cytoskeleton of the helical bacterium *Spiroplasma melliferum* BC3. *Mol. Microbiol.* **41**, 827–848 (2001).
24. Trachtenberg, S. The cytoskeleton of *Spiroplasma*: a complex linear motor. *J. Mol. Microbiol. Biotechnol.* **11**, 265–283 (2006).
25. Kurner, J., Frangakis, A. S. & Baumeister, W. Cryo-electron tomography reveals the cytoskeletal structure of *Spiroplasma melliferum*. *Science* **307**, 436–438 (2005).
26. Rohrbach, A. Stiffness of optical traps: quantitative agreement between experiment and electromagnetic theory. *Phys. Rev. Lett.* **95**, 168102 (2005).
27. Faucheux, L. P., Stolovitzky, G. & Libchaber, A. Periodic forcing of a Brownian particle. *Phys. Rev. E* **51**, 5239–5250 (1995).
28. Nambiar, R. & Meiners, J. C. Fast position measurements with scanning line optical tweezers. *Opt. Lett.* **27**, 836–838 (2002).
29. Neuman, K. C., Chadd, E. H., Liou, G. F., Bergman, K. & Block, S. M. Characterization of photodamage to *Escherichia coli* in optical traps. *Biophys. J.* **77**, 2856–2863 (1999).
30. Seitz, P. C., Stelzer, E. H. K. & Rohrbach, A. Interferometric tracking of optically trapped probes behind structured surfaces: a phase correction method. *Appl. Opt.* **45**, 7903–7915 (2006).
31. Born, M. & Wolf, E. *Principles of Optics* 5th edn (Cambridge Univ. Press, 1975).

Acknowledgements

The authors thank S. Trachtenberg, F. Hamprecht, J. Huisken and L. Friedrich for stimulating discussions, as well as J. Korvink, B. Tränkle, F. Fahrbach, F. Kohler, B. Landenberger and B. Bosworth for a careful reading of the manuscript. This study was supported by the Excellence Initiative of the German Federal and State Governments (EXC 294) and by the Deutsche Forschungsgemeinschaft (DFG) (grant nos RO 3615/1 and RO 3615/2).

Author contributions

M.K. performed experiments and simulations, analysed data and prepared all graphs. A.R. initiated and supervised the project, designed the system, developed the theory and wrote the manuscript.

Additional information

Supplementary information is available in the online version of the paper. Reprints and permission information is available online at <http://www.nature.com/reprints>. Correspondence and requests for materials should be addressed to A.R.

Competing financial interests

The authors declare no competing financial interests.